

Self-Navigated Residual Mamba for Universal Industrial Anomaly Detection

Hanxi Li^{1*}, Jingqi Wu^{2*}, Lin Yuanbo Wu³, Mingliang Li¹,
Deyin Liu⁴, Jialie Shen⁵, Chunhua Shen⁶

¹Jiangxi Normal University, China ²Southern University of Science and Technology

³Swansea University, United Kingdom ⁴Anhui University, China

⁵London University, United Kingdom ⁶Zhejiang University, China

Abstract

In this paper, we propose Self-Navigated Residual Mamba (SNARM), a novel framework for universal industrial anomaly detection that leverages “self-referential learning” within test images to enhance anomaly discrimination. Unlike conventional methods that depend solely on pre-trained features from normal training data, SNARM dynamically refines anomaly detection by iteratively comparing test patches against adaptively selected in-image references. Specifically, we first compute the “inter-residuals” features by contrasting test image patches with the training feature bank. Patches exhibiting small-norm residuals (indicating high normality) are then utilized as self-generated reference patches to compute “intra-residuals”, amplifying discriminative signals. These inter- and intra-residual features are concatenated and fed into a novel Mamba module with multiple heads, which are dynamically navigated by residual properties to focus on anomalous regions. Finally, AD results are obtained by aggregating the outputs of a self-navigated Mamba in an ensemble learning paradigm. Extensive experiments on MVTec AD, MVTec 3D, and VisA benchmarks demonstrate that SNARM achieves state-of-the-art (SOTA) performance, with notable improvements in all metrics, including Image-AUROC, Pixel-AURC, PRO, and AP. The source code are available in <https://github.com/BeJane/SNARM.git>

Introduction

Industrial Anomaly Detection (IAD) is crucial in modern manufacturing, ensuring product quality and reducing defects in automated production lines. However, the growing complexity of industrial processes poses significant challenges. Production lines increasingly handle diverse products, making the conventional category-specific anomaly detection (AD) models (Roth et al. 2022a; Zavrtanik, Kristan, and Skočaj 2021; Li et al. 2023a) impractical due to GPU memory and computational constraints. Therefore, the multi-class IAD problem has attracted significant research attention (Liu et al. 2021; Guo et al. 2024; He et al. 2024b). Additionally, the scarcity of training samples for every product category has spurred interest in few-shot IAD algorithms (Gu et al. 2023; Jeong et al. 2023; Damm et al. 2025). To address these challenges more elegantly, researchers have

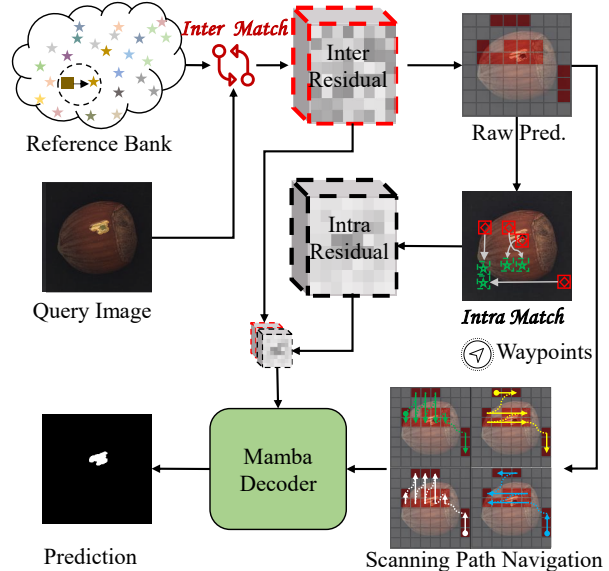


Figure 1: Illustration of the proposed Self-Navigated Residual Mamba (SNARM). Different from conventional residual-based AD methods, the patch matching in this work contains two stages: the inter-matching stage and the intra-matching stage. The raw-prediction, *i.e.*, the anomaly prediction based on the inter-matching guides the following intra-matching stage as well as the waypoint generation for navigating the scanning paths of the Mamba decoder.

recently pursued a unified framework—termed Universal Anomaly Detection (Univ-AD) (Luo et al. 2025)—which shows promising scalability and efficiency for real-world IAD tasks.

Recent advancements in deep learning have demonstrated the potential for Univ-AD tasks. Some recently-proposed IAD methods (Li et al. 2023b; Guo et al. 2024; Damm et al. 2025; Luo et al. 2025) leverage the modern architectures such Vision Transformers (ViT) (Zhang et al. 2023a) to capture long-range dependencies and hierarchical features for anomaly discrimination. On the contrary, as a well-acknowledged competitor of Transformers, Mamba (Gu and Dao 2023; Zhu et al. 2024) can generate comparable per-

*These authors contributed equally.

Copyright © 2026, Association for the Advancement of Artificial Intelligence (www.aaai.org). All rights reserved.

formance while at a lower computational cost. However, the Mamba-based IAD algorithms (He et al. 2024a; Iqbal and Martinel 2025) can hardly beat the Transformer based methods on most benchmarks. Customizing the Mamba framework for industrial AD remains an open challenge, particularly in refining feature representations and optimizing computational efficiency.

In this paper, we propose **Self-Navigated Residual Mamba (SNARM)**, a novel Univ-AD algorithm that achieves state-of-the-art performance through three core innovations. First, instead of relying on a conventional one-stage patch-matching scheme, SNARM adopts a two-stage residual matching process. In the first stage, test patches are matched against a memory bank built from anomaly-free images to generate initial residuals. In the second stage, these test patches are re-matched against low-confidence patches—those predicted as normal by the first stage—producing more refined second-order residuals. This self-referential procedure is termed **Intra-Matching**, while the initial inter-image matching is referred to as **Inter-Matching**. Together, they form a **Hybrid Matching** strategy that enhances detection accuracy and reduces memory bank size, improving overall efficiency. Second, we introduce a **Self-Navigated Mamba Module** tailored for anomaly localization. Its scanning paths are dynamically guided by the residual properties, enabling more effective focus on anomalous regions. Finally, we aggregate the outputs from multiple directional and scale-specific Mamba branches using an ensemble learning framework, enhancing the robustness and reliability of predictions. An overview of the proposed method, compared with conventional residual-based approaches, is illustrated in Fig. 1.

Our main contributions are summarized as follows:

- We propose **Hybrid Matching** for Univ-AD, where test patches participate in reference generation via self-referential matching, boosting both accuracy and efficiency.
- We design a **Self-Navigated Mamba Module** to enhance spatial focus on anomalies, and propose an ensemble-based decoder for robust multi-view integration.
- SNARM achieves state-of-the-art results on major benchmarks while maintaining high computational efficiency, making it suitable for real-world deployment.

Related Work

Industrial Anomaly Detection

The field of Industrial Anomaly Detection (IAD) has seen rapid advancements since the pioneering work (Venkataraman et al. 2020; Roth et al. 2022a; Chen et al. 2022) laid the foundation for modern IAD algorithms. Early research primarily focused on the single-class setting, where a dedicated model is trained for each product category. The representative works include CutPaste (Li et al. 2021), which leverages self-supervised learning for anomaly localization, DRAEM (Zavrtanik, Kristan, and Skočaj 2021) with its discriminative reconstruction embedding, and DRA (Ding,

Pang, and Shen 2022), which learns a disentangled representation for unseen anomalies. Other notable contributions, such as DeSTS (Zhang et al. 2023b), SimpleNet (Liu et al. 2023), and RealNet (Zhang, Xu, and Zhou 2024), further advanced single-class AD through techniques like segmentation-guided denoising, lightweight architectures, and realistic synthetic anomalies. As real-world industrial scenarios often involve multiple product categories, researchers shifted toward multi-class AD frameworks. Methods like works (Liu et al. 2021; Guo et al. 2024; He et al. 2024b) introduced scalable solutions for handling diverse categories within a single model, while exploring plain ViT (Zhang et al. 2023a) features demonstrated the potential of Vision Transformers in this setting. Another critical challenge is the scarcity of labeled anomalies, motivating research in few-shot AD. Works such as (Huang et al. 2022; Gu et al. 2023; Jeong et al. 2023; Damm et al. 2025) explored ways to detect anomalies with minimal supervision, either through visual or cross-modal cues. At the end of this spectrum lies universal AD, exemplified by the algorithm INP-Former (Luo et al. 2025), which aims to unify single-class, multi-class, and few-shot AD under a single framework. In this paper, our work builds upon these advancements to propose a more robust and scalable universal AD solution.

Mamba-based IAD algorithms

The recently proposed Mamba architecture (Gu and Dao 2023), inspired by State Space Models (Gu, Goel, and Ré 2021), has emerged as a competitive alternative to Transformer-based models, offering comparable performance with significantly lower computational complexity. This efficiency has spurred the development of numerous Mamba-based visual models (Liu et al. 2024; Pei, Huang, and Xu 2024; Wang et al. 2024; Zhu et al. 2024; Yang et al. 2025) tailored for various downstream tasks, including Industrial Anomaly Detection (IAD). For instance, Pyramid (Iqbal and Martinel 2025) adopts a Mamba model combined with a Pyramid Scanning Strategy to extract hierarchical features from CNN representations. Meanwhile, MambaAD (He et al. 2024a) introduces a Hybrid State Space block to integrate global context for anomaly detection while leveraging local features through traditional CNN modules. Although these methods demonstrate promising results in multi-class IAD, they still fall short of surpassing the performance achieved by advanced Transformer-based AD algorithms such as INP-Former (Luo et al. 2025) and Dino-omaly (Guo et al. 2024). In this work, we present a meticulously designed Mamba framework specifically optimized for universal IAD, achieving state-of-the-art performance across single-class, multi-class, and few-shot anomaly detection scenarios.

Method

Overview

We propose a novel residual-guided anomaly localization framework that enhances abnormality discrimination by integrating hybrid residual representations with dynamically

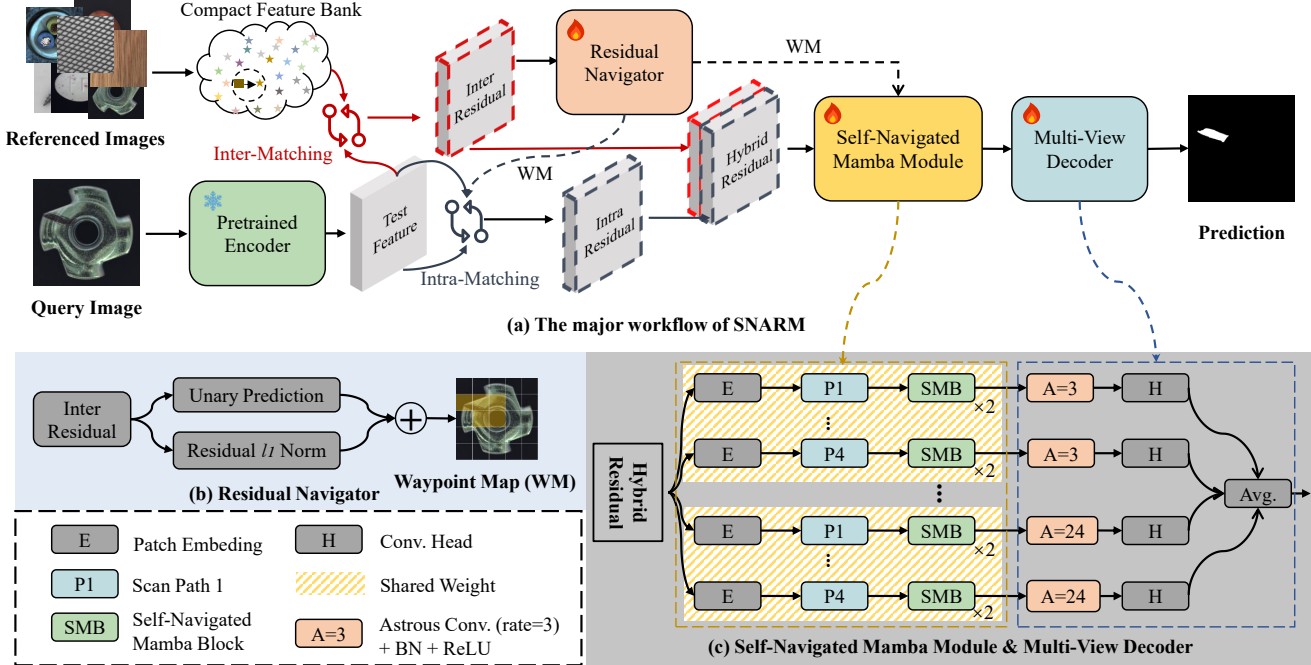


Figure 2: Overview of the proposed SNARM method. The query image is matched with an external feature bank to generate Inter-Residuals, followed by Inter-Matching to obtain Intra-Residuals. These are concatenated into Hybrid Residuals. A Waypoint Map (WM), derived from Inter-Residuals, dynamically guides the Self-Navigated Mamba Module to localize anomalies. Better viewed in color.

guided Mamba branches, as illustrated in Fig. 2. The framework comprises four key components: **Hybrid Matching (Hybrid-M)**, a **Self-Navigated Mamba Module (SNMM)**, a **Multi-View Decoder (MVD)**, and an **ensemble learning strategy**.

Hybrid Matching

We introduce a **Hybrid Matching (Hybrid-M)** strategy that integrates both *Inter-Matching* and *Intra-Matching*, guided by a Residual Navigator to effectively capture complementary normality patterns across images and within the test image itself.

Universal Visual Feature Extraction Inspired by the potential of foundation models (e.g., DINOv2-R (Darcel et al. 2023)) to provide general-purpose visual representations, we extract deep features from the input image $\mathbf{I} \in \mathbb{R}^{h_1 \times w_1 \times 3}$ using a pretrained encoder $\Psi_{\text{EN}}(\cdot)$:

$$\begin{aligned} \{\mathbf{F}^1, \mathbf{F}^2, \dots, \mathbf{F}^L\} &= \Psi_{\text{EN}}(\mathbf{I}) \\ \mathbf{F} &= \text{Concat} \left(\frac{2}{L} \sum_{l=1}^{L/2} \mathbf{F}^l, \frac{2}{L} \sum_{l=L/2+1}^L \mathbf{F}^l \right) \quad (1) \\ [\mathbf{f}_1, \mathbf{f}_2, \dots, \mathbf{f}_M] &= \text{Flatten}(\text{Up}(\mathbf{F})) \end{aligned}$$

Here, $\mathbf{F}^l \in \mathbb{R}^{h_f \times w_f \times d_f}$ denote the feature map from the l -th encoder block. We compute the average of early-layer (low-level) and late-layer (semantic) features, concatenate

them, and then apply adaptive pooling following (Roth et al. 2022a) to obtain a unified representation $\mathbf{F} \in \mathbb{R}^{h_f \times w_f \times d_f}$. This fused feature map is then upsampled and flattened into $M = h_f \cdot w_f$ local descriptors, denoted as $\mathbf{f}_i \in \mathbb{R}^{d_f}$.

Inter-Matching This Module aims to provide a consistent external reference for each test patch by querying a shared prototype bank. To construct this bank, we extract M patch features from each normal training image and collect them into a raw feature pool:

$$\mathcal{B}_{\text{raw}} = \{\mathbf{f}_{i,j}^{\text{ref}} \in \mathbb{R}^{d_f} \mid j = 1, \dots, N_{\text{trn}}, i = 1, \dots, M\}, \quad (2)$$

where N_{trn} is the number of training images. To reduce memory and computation costs, we apply a coresnet sampling algorithm (Roth et al. 2022a) to obtain a compact prototype bank:

$$\mathcal{B} = \Psi_{\text{core}}(\mathcal{B}_{\text{raw}}) = \{\mathbf{f}_t^{\text{ref}} \in \mathbb{R}^{d_f} \mid t = 1, \dots, T\}, \quad (3)$$

where $T \ll M \cdot N_{\text{trn}}$ and $\Psi_{\text{core}}(\cdot)$ denotes the coresnet selection function.

During inference, each test patch feature $\mathbf{f}_i^{\text{tst}}$ is matched with its nearest reference in the prototype bank using L_2 distance:

$$t^* = \arg \min_{t=1, \dots, T} \|\mathbf{f}_i^{\text{tst}} - \mathbf{f}_t^{\text{ref}}\|_2. \quad (4)$$

We then compute each patch of the Inter-Residual features $\mathbf{R} \in \mathbb{R}^{h_f \times w_f \times d_f}$ as a powered absolute difference:

$$\mathbf{r}_i = (\text{ABS}(\mathbf{f}_i^{\text{tst}} - \mathbf{f}_{t^*}^{\text{ref}}))^{\theta}, \quad \forall i, \quad (5)$$

where $\text{ABS}(\cdot)$ denotes the element-wise absolute difference, and the exponent $\theta \in \{1, 2\}$ is used to adjust the anomaly contrast level.

Intra-Matching Guided by Residual Navigator To improve matching fidelity and better highlight subtle anomalies, our method adaptively derives normal references from the test image itself. Unlike SoftPatch (Jiang et al. 2022) and FunAD (Im, Son, and Hong 2025), which leverage test features mainly for label denoising, or INP-Former (Luo et al. 2025), which lacks explicit control over matching granularity, SNARM introduces a dedicated and interpretable matching framework that explicitly separates and fuses global and local cues, enabling more accurate and robust anomaly localization.

Specifically, we introduce a **Residual Navigator** that produces a coarse anomaly confidence map, termed the **Waypoint Map (WM)**, which highlights spatial regions likely to be abnormal. These pseudo-reference anchors are then used to recalibrate the residual distribution and guide downstream modules to focus on informative areas.

Given the inter-residual features $\mathbf{R} \in \mathbb{R}^{h_f \times w_f \times d_f}$, the Residual Navigator consists of two parallel branches:

$$\mathbf{Q} = \sigma(\text{Conv}_{1 \times 1}(\mathbf{R})), \quad \mathbf{Q}^* = \mathbf{Q} + \frac{1}{d_f} \sum_{k=1}^{d_f} \mathbf{R}(i, j, k), \quad (6)$$

where $\text{Conv}_{1 \times 1}$ is a unary anomaly classifier composed of a 1×1 convolution followed by a sigmoid activation $\sigma(\cdot)$, and the second term computes the channel-wise average residual magnitude at each spatial location. The resulting \mathbf{Q}^* serves as the final Waypoint Map.

Then, we select a subset of reliable patches from the test image whose waypoint scores are among the lowest $p\%$. These low-score patches are assumed to be normal and are used as internal references for matching:

$$\mathcal{S} = \{ \mathbf{f}_k^{\text{tst}} \mid \mathbf{Q}^*(k) < \text{Percentile}(\mathbf{Q}^*, p) \}, \quad (7)$$

where $\mathbf{Q}^*(k)$ denotes the waypoint score of the k -th patch, and $\text{Percentile}(\cdot, p)$ returns the p -th percentile threshold across all test patches.

Each patch $\mathbf{f}_i^{\text{tst}}$ is re-matched with the closest trusted patch $\mathbf{f} \in \mathcal{S}$ to compute the **Intra-Residuals** $\tilde{\mathbf{R}} \in \mathbb{R}^{h_f \times w_f \times d_f}$:

$$\tilde{\mathbf{r}}^* = \arg \min_{\mathbf{f} \in \mathcal{S}} \|\mathbf{f}_i^{\text{tst}} - \mathbf{f}\|_2, \quad \tilde{\mathbf{r}}_i = (\text{ABS}(\mathbf{f}_i^{\text{tst}} - \mathbf{f}_{\tilde{\mathbf{r}}^*}))^\theta. \quad (8)$$

Finally, we concatenate the inter-residuals and intra-residuals to form the **Hybrid Residuals** $\hat{\mathbf{R}} \in \mathbb{R}^{h_f \times w_f \times 2d_f}$:

$$\hat{\mathbf{R}} = [\mathbf{R} \parallel \tilde{\mathbf{R}}], \quad (9)$$

which encodes both global abnormality deviation and refined self-referenced differences.

Self-Navigated Mamba Module

Mamba (Gu and Dao 2023) has shown strong potential for capturing long-range dependencies via state-space modeling. However, directly applying it to dense anomaly localization is computationally expensive and less effective due to the large number of spatial tokens.

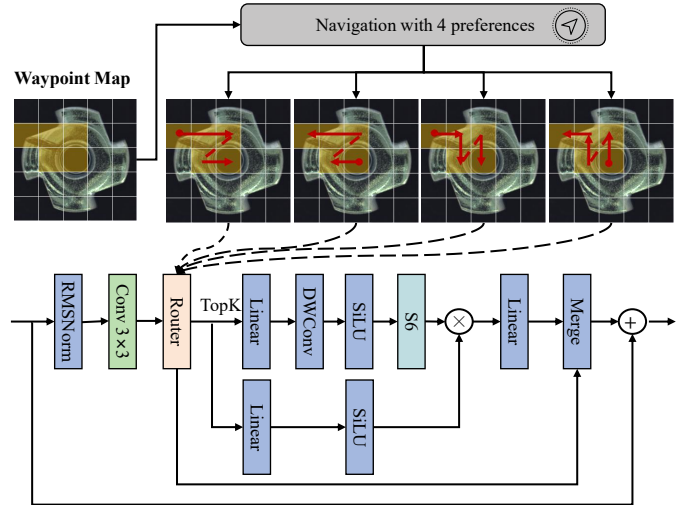


Figure 3: Overview of the proposed **Self-Navigated Mamba Block (SMB)**. Guided by the Waypoint Map, the block selectively scans informative regions using four directional passes, enabling efficient and spatially-aware message propagation over reduced token sets. Better viewed in color.

To address this, we propose the **Self-Navigated Mamba Block (SMB)**, which dynamically selects a compact and informative subset of tokens based on the Waypoint Map, as shown in Fig. 3. To enhance spatial perception, SMB performs directional scanning in four orientations—left-to-right, right-to-left, top-down, and bottom-up—allowing better contextual aggregation across axes. To further enrich local context and propagate anomaly cues, a 3×3 convolutional layer is placed before each scan.

The complete **Self-Navigated Mamba Module (SNMM)** consists of a feature embedding layer followed by two stacked SMBs. Given the hybrid-residual features, SNMM generates four directionally-aware outputs $\{\mathbf{o}^{(\rightarrow)}, \mathbf{o}^{(\leftarrow)}, \mathbf{o}^{(\downarrow)}, \mathbf{o}^{(\uparrow)}\}$, which are passed to the decoder for final anomaly prediction.

Multi-View Decoder

In IAD, anomalies vary significantly in scale, shape, and contextual appearance—ranging from subtle scratches to large structural defects. To robustly capture such heterogeneous patterns, we introduce a **Multi-View Decoder (MVD)**, composed of multiple **View-Specific Branches**, each tailored to a distinct spatial perspective (multi-scan and multi-scale), as illustrated in Fig. 2(c).

Each branch receives a directional feature map $\mathbf{o}^{(d)}$ from the SNMM, where $d \in \{\rightarrow, \leftarrow, \downarrow, \uparrow\}$ denotes the scan direction. To enhance adaptability to varying anomaly scales, we employ a branch-specific Atrous Convolution Block $\mathcal{A}_{r,d}(\cdot)$ with a unique dilation rate $r \in \{3, 6, 12, 24\}$:

$$\tilde{\mathbf{o}}^{(r,d)} = \mathcal{A}_{r,d}(\mathbf{o}^{(d)}) = \text{AtrousConv}(\mathbf{o}^{(d)}; r). \quad (10)$$

The transformed features are then passed through a lightweight prediction head $\mathcal{H}(\cdot)$, which comprises a 1×1

convolution, an upsampling operation, and a Sigmoid activation $\sigma(\cdot)$ to produce the anomaly map:

$$\mathbf{m}^{(r,d)} = \mathcal{H}(\tilde{\mathbf{o}}^{(r,d)}) = \sigma \left(\text{Up} \left(\text{Conv}_{1 \times 1}(\tilde{\mathbf{o}}^{(r,d)}) \right) \right), \quad (11)$$

where $\mathbf{m}^{(r,d)}$ denotes the anomaly probability map corresponding to view d and dilation rate r .

Ensemble Learning Strategy

Cyclic Optimization and Loss Function An iterative training strategy is adopted to promote diversity among the *View-Specific Branches*. Specifically, we sequentially update one branch at a time for \mathcal{K} steps while freezing the others.

We adopt the Focal Loss (Lin et al. 2017) to supervise both the Residual Navigator and the Multi-View Decoder. During each cycle, only the active branch contributes to the training loss, while the Residual Navigator is jointly optimized across the entire training process. The total loss $\mathcal{L}_{\text{total}}$ at each training iteration is as follow:

$$\mathcal{L}_{\text{total}} = \mathcal{L}_{\text{focal}}(\text{Up}(\mathbf{Q}), \mathbf{Y}) + \frac{1}{4} \sum_{j=1}^4 \mathcal{L}_{\text{focal}}(\mathbf{m}^{i,j}, \mathbf{Y}), \quad (12)$$

where $\text{Up}(\cdot)$ denotes a bilinear interpolation operation that resizes the low-resolution output \mathbf{Q} from the Residual Navigator’s convolution branch in Equ. 6 to the original input resolution of the ground truth map $\mathbf{Y} \in \{0, 1\}^{h_I \times w_I}$. $\mathbf{m}^{i,j}$ is the anomaly prediction from the j -th directional sub-branch of the i -th scale-specific branch, and $\mathcal{L}_{\text{focal}}(\cdot)$ is the Focal Loss (Lin et al. 2017) defined as:

$$\begin{aligned} \mathcal{L}_{\text{focal}}(\hat{\mathbf{M}}, \mathbf{Y}) = & - \sum_{x,y} [\alpha(1 - \hat{\mathbf{M}}_{x,y})^\gamma \mathbf{Y}_{x,y} \log(\hat{\mathbf{M}}_{x,y}) \\ & + (1 - \alpha)\hat{\mathbf{M}}_{x,y}^\gamma (1 - \mathbf{Y}_{x,y}) \log(1 - \hat{\mathbf{M}}_{x,y})], \end{aligned} \quad (13)$$

where $\hat{\mathbf{M}}_{x,y}$ denotes the predicted probability at pixel location (x, y) , α is the weighting factor for class imbalance, and γ is the focusing parameter to down-weight easy examples.

Feature Augmentation Strategies To improve the robustness and generalization of the model, we introduce two feature augmentation strategies tailored for residual-based anomaly detection.

(1) Top- k Feature Averaging In conventional residual computation, $\mathbf{f}_{t^*}^{\text{ref}}$ is the most similar reference feature from the memory bank \mathcal{B} when computing the Inter-Residual features according to Equ. 5. We extend this by averaging the top- k nearest features $\{\mathbf{f}_{t_1}, \dots, \mathbf{f}_{t_k}\}$ to form a more stable reference:

$$\mathbf{f}_i^{\text{ref}} = \frac{1}{k} \sum_{j=1}^k \mathbf{f}_{t_j}. \quad (14)$$

This approach smooths residual computation, mitigating the effect of noise. It can be applied during both training and inference stages.

(2) Consistent Feature Jittering Inspired by Feature Jittering in UniAD (You et al. 2022), we introduce a *noise-consistent* augmentation mechanism. Specifically, we sample a noise vector $\epsilon \sim \mathcal{N}(0, \mathbf{I})$ for each sample and add it

to both its universal visual feature \mathbf{f}_i and its Inter-Residual feature \mathbf{r}_i , ensuring consistency in perturbation:

$$\tilde{\mathbf{f}}_i = \mathbf{f}_i + \lambda \frac{\|\mathbf{f}_i\|_2}{d_f} \epsilon, \quad \tilde{\mathbf{r}}_i = \mathbf{r}_i + \lambda \frac{\|\mathbf{r}_i\|_2}{d_f} \epsilon \quad \forall i. \quad (15)$$

where λ is the jittering scale to control the noisy degree.

Inference The final anomaly map is obtained by averaging the outputs from all 4×4 view-specific branches:

$$\hat{\mathbf{m}} = \frac{1}{16} \sum_{i=1}^4 \sum_{j=1}^4 \mathbf{m}^{i,j}, \quad (16)$$

where $\hat{\mathbf{m}} \in [0, 1]^{h_I \times w_I}$ denotes the aggregated confidence map, and $\mathbf{m}^{i,j}$ denotes the anomaly prediction from the j -th directional sub-branch of the i -th scale-specific branch.

Implementation Details

SNARM employs ViT-Base/14 with DINoV2-R (Darcel et al. 2023) weights as the default pre-trained encoder $\Psi_{\text{EN}}(\cdot)$. Feature maps are extracted from the intermediate outputs of the 1st to 8th transformer blocks. Input images are first resized to 448×448 and then center-cropped to 392×392 . The training hyperparameters are set as follows: $T = 10^4$ in Eq.3, $p = 75$ in Eq.7, $k = 3$ in Eq. 14, $\mathcal{K} = 100$, and $\lambda = 30$. For the Residual Navigator loss, we use $\alpha = 0.5$ and $\gamma = 4$, while for the View-Specific Branch loss, we set $\alpha = 0.25$ and $\gamma = 4$. The entire framework is optimized using the Adam optimizer with a learning rate of 0.001 and a weight decay of 0.05. All experiments are conducted on a single PC equipped with an Intel i5-13450 CPU, 64GB RAM, and an NVIDIA RTX 4090 GPU.

Experiments

Experimental Setting

The experiments are conducted on three widely-used benchmarks: the MVTec-AD (Bergmann et al. 2019) MVTec-3D (Bergmann et al. 2021) and VisA (Zou et al. 2022) datasets. To ensure a fair and comprehensive evaluation, we adopt four threshold-independent metrics: Image-level AUROC (I-AUROC), Pixel-level AUROC (P-AUROC), Per-Region Overlap (PRO), and Average Precision (P-AP). Among them, I-AUROC assesses the accuracy of anomaly detection at the image level, while P-AUROC, PRO, and P-AP evaluate the performance of anomaly localization.

Results under the Multi-Class Setting

As shown in Table 1, SNARM achieves state-of-the-art or highly competitive results across all three datasets, even with a highly compact memory bank. On MVTec-AD (Bergmann et al. 2019), it achieves superior pixel-level performance **(79.0/96.6/99.1)** and a competitive I-AUROC, surpassing prior best results by **1.9/1.7/0.6**. On the more challenging MVTec-3D (Bergmann et al. 2021), SNARM achieves **63.6/97.4/99.2/93.9**, outperforming previous methods by margins of **7.7/0.4/0.0/1.3**. Similarly, on VisA (Zou et al. 2022), it attains **55.8/94.7/99.1** with a competitive I-AUROC, improving over prior results by **2.6/0.2/10.2**. Notably, reducing the memory bank size has minimal impact

Dataset	MVTec-AD (Bergmann et al. 2019)				MVTec-3D (Bergmann et al. 2021)				VisA (Zou et al. 2022)			
Method	P_AP	PRO	P_AUROC	I_AUROC	P_AP	PRO	P_AUROC	I_AUROC	P_AP	PRO	P_AUROC	I_AUROC
RD4AD (Deng and Li 2022)	48.6	91.1	96.1	94.6	29.8	93.5	98.4	77.9	38.0	91.8	98.1	92.4
UniAD (You et al. 2022)	43.4	90.7	96.8	96.5	21.2	88.1	96.5	78.9	33.7	85.5	98.3	88.8
SimpleNet (Liu et al. 2023)	45.9	86.5	96.9	95.3	18.3	77.6	93.5	72.5	34.7	81.4	96.8	87.2
DeSTSeg (Zhang et al. 2023b)	54.3	64.8	93.1	89.2	38.1	46.4	95.1	79.6	39.6	67.4	96.1	88.9
DiAD (He et al. 2024b)	52.6	90.7	96.8	97.2	25.3	87.8	96.4	84.6	26.1	75.2	96.0	86.8
MambaAD (He et al. 2024a)	56.3	93.1	97.7	98.6	37.5	93.6	98.6	86.2	39.4	91.0	98.5	94.3
WeakREST (Li et al. 2023b)	77.1	95.4	98.3	98.5	48.8	95.4	98.6	83.8	~	~	~	~
CPR (Li et al. 2023a)	63.3	93.1	97.2	95.7	37.6	95.2	98.4	80.9	~	~	~	~
Dinomaly (Guo et al. 2024)	68.7	94.7	98.3	99.6	55.0	96.5	99.2	90.6	53.2	94.5	98.7	98.7
INP-Former (Luo et al. 2025)	71.0	94.9	98.5	99.7	55.9	97.0	99.2	92.6	51.2	94.4	98.9	98.9
SNARM ($T = 10^4$)	76.9	95.9	98.9	99.1	59.5	96.5	99.0	90.2	55.6	90.1	98.4	96.8
SNARM ($T = 10^5$)	79.0	96.6	99.1	99.4	63.6	97.4	99.2	93.9	55.8	94.7	99.1	98.1

Table 1: **Multi-class** anomaly detection performance on different AD datasets. The best accuracy in one comparison with the same data and metric condition is shown in **red** while the second one is shown in **blue**.

Dataset	MVTec-AD (Bergmann et al. 2019)				MVTec-3D (Bergmann et al. 2021)				VisA (Zou et al. 2022)			
Method	P_AP	PRO	P_AUROC	I_AUROC	P_AP	PRO	P_AUROC	I_AUROC	P_AP	PRO	P_AUROC	I_AUROC
PaDiM (Defard et al. 2021)	53.6	92.2	97.3	95.5	23.7	91.0	97.3	76.6	31.3	83.6	97.6	89.9
PatchCore (Roth et al. 2022a)	57.1	93.1	98.1	99.1	26.3	89.1	97.0	82.5	39.5	86.2	97.8	90.4
CPR (Li et al. 2023a)	61.4	91.4	96.8	92.8	23.6	87.6	96.3	71.3	30.8	77.5	92.7	87.8
HETMM (Chen et al. 2024)	68.0	95.8	98.6	99.2	37.7	94.8	98.4	83.4	38.4	89.1	96.3	89.0
Dinomaly (Guo et al. 2024)	15.2	39.5	73.8	63.6	4.2	59.5	87.8	46.9	9.8	51.5	86.3	59.5
SNARM ($T = 10^4$)	78.4	96.1	99.0	99.3	68.9	97.3	99.1	94.5	56.0	93.8	99.1	98.0

Table 2: **Cross-class** anomaly detection performance on different AD datasets.

on performance, highlighting the robustness and efficiency of our framework. Detailed per-class results are provided in the Supplementary Material.

Results under the Cross-Class Setting

In this setting, models are evaluated on previously unseen classes without additional retraining. For embedding-based methods (e.g., PatchCore (Roth et al. 2022a), PaDiM (Defard et al. 2021), HETMM (Chen et al. 2024)), we employ a backbone pre-trained on a large-scale dataset such as ImageNet (Russakovsky et al. 2015). For learning-based methods (e.g., SNARM, Dinomaly (Guo et al. 2024) and CPR (Li et al. 2023a)), we adopt a leave-one-out strategy, where one class is designated for testing while the remaining classes are used for training.

As shown in Table 2, our method achieves best-in-class performance across all benchmarks. On MVTec-AD (Bergmann et al. 2019), it attains scores of **78.4/96.1/99.0/99.3**, outperforming the previous best by **10.4/0.3/0.4/0.1**, respectively. For MVTec-3D (Bergmann et al. 2021), our method reaches **68.9/97.3/99.1/94.5**, with margins of **31.2/2.5/0.7/11.1** over the prior state-of-the-art. Similarly, on VisA (Zou et al. 2022), it achieves **56.0/93.8/99.1/98.0**, surpassing existing methods by **16.5/4.7/1.3/7.6**, further validating its strong generalization and effectiveness. Detailed per-class results are provided in the Supplementary Material.

Results under the Single-Class Setting

As presented in Table 3, SNARM delivers state-of-the-art or highly competitive performance across all three

benchmarks under the Single-class setting. On MVTec-AD (Bergmann et al. 2019), SNARM achieves outstanding pixel-level scores of **79.2/96.6/99.0**, exceeding previous best results by **9.0/1.2/0.7**. On MVTec-3D (Bergmann et al. 2021), our method reaches **65.5/97.2/99.2/94.0**, surpassing prior approaches by margins of **8.9/0.2/0.0/1.0**. On the VisA dataset (Zou et al. 2022), SNARM also demonstrates competitive performance. Detailed per-category metrics are provided in the Supplementary Material.

Results under the Few-Shot Setting

As shown in Table 4, SNARM achieves state-of-the-art or highly competitive performance under the few-shot setting. On MVTec-AD (Bergmann et al. 2019), it obtains impressive scores of **68.6/94.6/97.9/98.3**, outperforming previous methods by margins of **2.7/1.7/0.9/0.7**. On the VisA dataset (Zou et al. 2022), SNARM also achieves strong and competitive results.

Complexity Comparisons

Table 6 compares SNARM with recent state-of-the-art methods in terms of efficiency. SNARM achieves the best mAD score (92.7) with only 69 GFLOPs, 68.3M parameters, and competitive speed (48 FPS), offering an excellent trade-off between accuracy and complexity.

Ablation Study

We conduct an ablation study on the MVTec-AD dataset (Bergmann et al. 2019) under multi-class and few-shot settings (Table 5). Starting from the base model with

Dataset	MVTec-AD (Bergmann et al. 2019)				MVTec-3D (Bergmann et al. 2021)				VisA (Zou et al. 2022)			
Method	P_AP	PRO	P_AUROC	I_AUROC	P_AP	PRO	P_AUROC	I_AUROC	P_AP	PRO	P_AUROC	I_AUROC
RD4AD (Deng and Li 2022)	58.0	93.9	97.8	98.0 ~	~	~	~	~	27.7	70.9		96.0
SimpleNet (Liu et al. 2023)	54.8	90.0	97.7	99.6	~	~	~	~	36.3	88.7		96.8
Dinomaly (Guo et al. 2024)	68.9	95.0	~	99.7	~	~	~	~	50.7	95.1		98.9
INP-Former (Luo et al. 2025)	70.2	95.4	98.3	99.7	56.6	97.0	99.2	93.0	49.2	93.8	98.4	98.5
SNARM ($T = 10^4$)	79.2	96.6	99.0	99.3	65.5	97.2	99.2	94.0	55.4	92.3	99.0	98.0

Table 3: **Single-class** anomaly detection performance on different AD datasets.

Dataset	MVTec-AD (Bergmann et al. 2019)				VisA (Zou et al. 2022)			
Method	P_AP	PRO	P_AUROC	I_AUROC	P_AP	PRO	P_AUROC	I_AUROC
PaDiM(Defard et al. 2021)	~	81.3	92.6	80.4	~	72.6	93.2	72.8
PatchCore (Roth et al. 2022b)	~	84.3	94.3	88.8	~	84.9	96.8	85.3
WinCLIP (Jeong et al. 2023)	~	89.0	96.2	95.2	~	87.6	97.2	87.3
PromptAD (Li et al. 2024)	~	90.5	96.5	96.6	~	86.2	97.4	89.1
AnomalyDINO (Damm et al. 2025)	~	92.4	96.7	97.6	~	92.5	98.0	91.3
INP-Former (Luo et al. 2025)	65.9	92.9	97.0	97.6	49.3	93.1	97.7	96.4
SNARM ($T = 10^4$)	68.6	94.6	97.9	98.3	49.5	92.9	98.1	94.5

Table 4: **Few-shot (4-shot)** anomaly detection performance on different AD datasets.

Module	Multi-Class				Few-Shot			
	P_AP	PRO	P_AUROC	I_AUROC	P_AP	PRO	P_AUROC	I_AUROC
Hybrid-M	SMB	MVD	TopK	Jitter	CT	70.2	93.8	97.7
✓						71.5	93.5	97.9
✓	✓					73.8	94.4	98.3
✓	✓	✓				76.9	95.3	98.8
✓	✓	✓	✓			77.5	95.7	98.8
✓	✓	✓	✓	✓		77.5	95.6	98.9
✓	✓	✓	✓	✓	✓	76.9	95.9	98.9

Table 5: Ablation on the MVTec-AD (Bergmann et al. 2019) dataset under the Multi-class and Few-shot (4-shot) settings.

Method	Params (M)	FLOPs(G)	FPS	mAD
DeSTSeg (Zhang et al. 2023b)	35.2	122.7	125	75.4
SimpleNet (Liu et al. 2023)	72.8	16.1	62	81.2
MambaAD (He et al. 2024a)	25.7	8.3	59	86.4
Dinomaly (Guo et al. 2024)	132.8	104.7	59	90.3
INP-Former (Luo et al. 2025)	139.8	98.0	38	91.0
SNARM ($T = 10^4$)	68.3	69.0	48	92.7

Table 6: Comparison of computational efficiency among SOTA methods. mAD represents the average value of four metrics under Multi-class setting on the MVTec-AD (Bergmann et al. 2019) dataset.

Inter-Residuals and vanilla Mamba, we first add **Hybrid-Matching (Hybrid-M)**, which significantly boosts performance by injecting informative Intra-Residuals. Integrating the **Self-Navigated Mamba Block (SMB)** further enhances anomaly localization via guided attention. Introducing the **Multi-View Decoder (MVD)** strengthens spatial adaptability across varied view. Then, the **Top- k Feature Averaging (TopK)** module improves robustness, the **Consistent Feature Jittering (Jitter)** introduces beneficial noise, and finally, **Cyclic Training (CT)** promotes diversity across view-specific branches, achieving the best overall results. Each component contributes progressively to the final model’s superior performance.

Conclusion
This work advances Universal Anomaly Detection (Univ-AD) by rethinking the adaptation of state-of-the-art deep learning frameworks for this downstream task, which innovatively makes use of residual features to enable anomaly detection. We introduce self-referential patch-matching, a dynamic process that generates “intra-residuals” while simultaneously pruning redundant computations, achieving both higher discrimination power and efficiency. Furthermore, the proposed Self-Navigated Mamba Blocks tailor scanning paths to anomaly contexts, and the multi-view decoder consolidates these features for robust predictions. The proposed algorithm, Self-Navigated Residual Mamba (SNARM), sets new performance records across MVTec AD, MVTec 3D, and VisA datasets against metrics (including Image-AUROC, Pixel-AUROC, PRO, AP) while maintaining real-world deployability. By unifying accuracy and practicality, SNARM addresses a fundamental industrial need: scalable, category-agnostic anomaly detection under resource constraints.

References

Bergmann, P.; Fauser, M.; Sattlegger, D.; and Steger, C. 2019. MVTec AD—A comprehensive real-world dataset for unsupervised anomaly detection. In *Proceedings of*

the IEEE/CVF conference on computer vision and pattern recognition, 9592–9600.

Bergmann, P.; Jin, X.; Sattlegger, D.; and Steger, C. 2021. The mvtec 3d-ad dataset for unsupervised 3d anomaly detection and localization. *arXiv preprint arXiv:2112.09045*.

Chen, Y.; Tian, Y.; Pang, G.; and Carneiro, G. 2022. Deep one-class classification via interpolated gaussian descriptor. In *Proceedings of the AAAI Conference on Artificial Intelligence*, volume 36, 383–392.

Chen, Z.; Xie, X.; Yang, L.; and Lai, J.-H. 2024. Hard-Normal Example-Aware Template Mutual Matching for Industrial Anomaly Detection. *International Journal of Computer Vision*, 1–23.

Damm, S.; Laszkiewicz, M.; Lederer, J.; and Fischer, A. 2025. Anomalydino: Boosting patch-based few-shot anomaly detection with dinov2. In *2025 IEEE/CVF Winter Conference on Applications of Computer Vision (WACV)*, 1319–1329. IEEE.

Darcet, T.; Oquab, M.; Mairal, J.; and Bojanowski, P. 2023. Vision transformers need registers. *arXiv preprint arXiv:2309.16588*.

Defard, T.; Setkov, A.; Loesch, A.; and Audigier, R. 2021. Padim: a patch distribution modeling framework for anomaly detection and localization. In *Pattern Recognition. ICPR International Workshops and Challenges: Virtual Event, January 10–15, 2021, Proceedings, Part IV*, 475–489. Springer.

Deng, H.; and Li, X. 2022. Anomaly detection via reverse distillation from one-class embedding. In *Proceedings of the IEEE/CVF Conference on Computer Vision and Pattern Recognition*, 9737–9746.

Ding, C.; Pang, G.; and Shen, C. 2022. Catching both gray and black swans: Open-set supervised anomaly detection. In *Proceedings of the IEEE/CVF Conference on Computer Vision and Pattern Recognition*, 7388–7398.

Gu, A.; and Dao, T. 2023. Mamba: Linear-time sequence modeling with selective state spaces. *arXiv preprint arXiv:2312.00752*.

Gu, A.; Goel, K.; and Ré, C. 2021. Efficiently modeling long sequences with structured state spaces. *arXiv preprint arXiv:2111.00396*.

Gu, Z.; Zhu, B.; Zhu, G.; Chen, Y.; Tang, M.; and Wang, J. 2023. AnomalyGPT: Detecting Industrial Anomalies using Large Vision-Language Models. ArXiv:2308.15366 [cs].

Guo, J.; Lu, S.; Zhang, W.; and Li, H. 2024. Dinomaly: The Less Is More Philosophy in Multi-Class Unsupervised Anomaly Detection. *arXiv e-prints*.

He, H.; Bai, Y.; Zhang, J.; He, Q.; Chen, H.; Gan, Z.; Wang, C.; Li, X.; Tian, G.; and Xie, L. 2024a. Mambaad: Exploring state space models for multi-class unsupervised anomaly detection. *arXiv e-prints*.

He, H.; Zhang, J.; Chen, H.; Chen, X.; Li, Z.; Chen, X.; Wang, Y.; Wang, C.; and Xie, L. 2024b. A diffusion-based framework for multi-class anomaly detection. In *AAAI*, volume 38, 8472–8480.

Huang, C.; Guan, H.; Jiang, A.; Zhang, Y.; Spratling, M.; and Wang, Y.-F. 2022. Registration based few-shot anomaly detection. In *Computer Vision–ECCV 2022: 17th European Conference, Tel Aviv, Israel, October 23–27, 2022, Proceedings, Part XXIV*, 303–319. Springer.

Im, J.; Son, Y.; and Hong, J. H. 2025. FUN-AD: Fully Unsupervised Learning for Anomaly Detection with Noisy Training Data. In *2025 IEEE/CVF Winter Conference on Applications of Computer Vision (WACV)*, 9447–9456. IEEE.

Iqbal, N.; and Martinel, N. 2025. Pyramid-based Mamba Multi-class Unsupervised Anomaly Detection. *arXiv preprint arXiv:2504.03442*.

Jeong, J.; Zou, Y.; Kim, T.; Zhang, D.; Ravichandran, A.; and Dabeer, O. 2023. Winclip: Zero-/few-shot anomaly classification and segmentation. In *Proceedings of the IEEE/CVF Conference on Computer Vision and Pattern Recognition*, 19606–19616.

Jiang, X.; Liu, J.; Wang, J.; Nie, Q.; Wu, K.; Liu, Y.; Wang, C.; and Zheng, F. 2022. Softpatch: Unsupervised anomaly detection with noisy data. *Advances in Neural Information Processing Systems*, 35: 15433–15445.

Li, C.-L.; Sohn, K.; Yoon, J.; and Pfister, T. 2021. Cutpaste: Self-supervised learning for anomaly detection and localization. In *Proceedings of the IEEE/CVF Conference on Computer Vision and Pattern Recognition*, 9664–9674.

Li, H.; Hu, J.; Li, B.; Chen, H.; Zheng, Y.; and Shen, C. 2023a. Target before shooting: Accurate anomaly detection and localization under one millisecond via cascade patch retrieval. *arXiv preprint arXiv:2308.06748*.

Li, H.; Wu, J.; Wu, L. Y.; Chen, H.; Liu, D.; Wang, M.; and Wang, P. 2023b. Industrial Anomaly Detection and Localization Using Weakly-Supervised Residual Transformers. *arXiv preprint arXiv:2306.03492*.

Li, X.; Zhang, Z.; Tan, X.; Chen, C.; Qu, Y.; Xie, Y.; and Ma, L. 2024. PromptAD: Learning Prompts with only Normal Samples for Few-Shot Anomaly Detection. In *Proceedings of the IEEE/CVF Conference on Computer Vision and Pattern Recognition (CVPR)*, 16838–16848.

Lin, T.-Y.; Goyal, P.; Girshick, R.; He, K.; and Dollár, P. 2017. Focal loss for dense object detection. In *Proceedings of the IEEE international conference on computer vision*, 2980–2988.

Liu, Y.; Tian, Y.; Zhao, Y.; Yu, H.; Xie, L.; Wang, Y.; Ye, Q.; Jiao, J.; and Liu, Y. 2024. Vmamba: Visual state space model. *Advances in neural information processing systems*, 37: 103031–103063.

Liu, Z.; Lin, Y.; Cao, Y.; Hu, H.; Wei, Y.; Zhang, Z.; Lin, S.; and Guo, B. 2021. Swin transformer: Hierarchical vision transformer using shifted windows. In *Proceedings of the IEEE/CVF international conference on computer vision*, 10012–10022.

Liu, Z.; Zhou, Y.; Xu, Y.; and Wang, Z. 2023. SimpleNet: A Simple Network for Image Anomaly Detection and Localization. In *Proceedings of the IEEE/CVF Conference on Computer Vision and Pattern Recognition (CVPR)*, 20402–20411.

Luo, W.; Cao, Y.; Yao, H.; Zhang, X.; Lou, J.; Cheng, Y.; Shen, W.; and Yu, W. 2025. Exploring Intrinsic Normal Prototypes within a Single Image for Universal Anomaly Detection. In *Proceedings of the IEEE/CVF Conference on Computer Vision and Pattern Recognition (CVPR)*.

Pei, X.; Huang, T.; and Xu, C. 2024. Efficientmamba: Atrous selective scan for light weight visual mamba. *arXiv preprint arXiv:2403.09977*.

Roth, K.; Pemula, L.; Zepeda, J.; Schölkopf, B.; Brox, T.; and Gehler, P. 2022a. Towards total recall in industrial anomaly detection. In *Proceedings of the IEEE/CVF Conference on Computer Vision and Pattern Recognition*, 14318–14328.

Roth, K.; Pemula, L.; Zepeda, J.; Schölkopf, B.; Brox, T.; and Gehler, P. 2022b. Towards Total Recall in Industrial Anomaly Detection. *ArXiv:2106.08265* [cs].

Russakovsky, O.; Deng, J.; Su, H.; Krause, J.; Satheesh, S.; Ma, S.; Huang, Z.; Karpathy, A.; Khosla, A.; Bernstein, M.; et al. 2015. Imagenet large scale visual recognition challenge. *International journal of computer vision*, 115: 211–252.

Venkataramanan, S.; Peng, K.-C.; Singh, R. V.; and Mahalanobis, A. 2020. Attention guided anomaly localization in images. In *Computer Vision–ECCV 2020: 16th European Conference, Glasgow, UK, August 23–28, 2020, Proceedings, Part XVII*, 485–503. Springer.

Wang, F.; Wang, J.; Ren, S.; Wei, G.; Mei, J.; Shao, W.; Zhou, Y.; Yuille, A.; and Xie, C. 2024. Mambarr: Vision mamba also needs registers. *arXiv preprint arXiv:2405.14858*.

Yang, N.; Wang, Y.; Liu, Z.; Li, M.; An, Y.; and Zhao, X. 2025. SMamba: Sparse Mamba for Event-based Object Detection. In *Proceedings of the AAAI Conference on Artificial Intelligence*, volume 39, 9229–9237.

You, Z.; Cui, L.; Shen, Y.; Yang, K.; Lu, X.; Zheng, Y.; and Le, X. 2022. A unified model for multi-class anomaly detection. *NeurIPS*, 35: 4571–4584.

Zavrtanik, V.; Kristan, M.; and Skočaj, D. 2021. DRAEM-a discriminatively trained reconstruction embedding for surface anomaly detection. In *Proceedings of the IEEE/CVF International Conference on Computer Vision*, 8330–8339.

Zhang, J.; Chen, X.; Wang, Y.; Wang, C.; Liu, Y.; Li, X.; Yang, M.-H.; and Tao, D. 2023a. Exploring plain vit reconstruction for multi-class unsupervised anomaly detection. *arXiv e-prints*.

Zhang, X.; Li, S.; Li, X.; Huang, P.; Shan, J.; and Chen, T. 2023b. DeSTSeg: Segmentation Guided Denoising Student-Teacher for Anomaly Detection. In *Proceedings of the IEEE/CVF Conference on Computer Vision and Pattern Recognition (CVPR)*, 3914–3923.

Zhang, X.; Xu, M.; and Zhou, X. 2024. Realnet: A feature selection network with realistic synthetic anomaly for anomaly detection. In *Proceedings of the IEEE/CVF Conference on Computer Vision and Pattern Recognition*, 16699–16708.

Zhu, L.; Liao, B.; Zhang, Q.; Wang, X.; Liu, W.; and Wang, X. 2024. Vision mamba: Efficient visual representation learning with bidirectional state space model. *arXiv preprint arXiv:2401.09417*.

Zou, Y.; Jeong, J.; Pemula, L.; Zhang, D.; and Dabeer, O. 2022. SPot-the-Difference Self-Supervised Pre-training for Anomaly Detection and Segmentation. *ArXiv:2207.14315* [cs].

Appendix

Per-Class Quantitative Results in the Multi-Class Setting

We report the per-class performance of our method on the MVTec-AD (Bergmann et al. 2019), MVTec-3D (Bergmann et al. 2021), and VisA (Zou et al. 2022) datasets under the multi-class anomaly detection setting. Results of the comparison methods are drawn from MambaAD (He et al. 2024a) and INP-Former (Luo et al. 2025). Table 10 summarizes the image-level anomaly detection and pixel-level localization performance on MVTec-AD, while Table 11 and Table 12 present the corresponding results on MVTec-3D and VisA. These results highlight the consistent superiority of our approach across diverse object categories.

Per-Class Quantitative Results in the Cross-Class Setting

We further evaluate per-class performance in the cross-class anomaly detection setting using the MVTec-AD, MVTec-3D, and VisA datasets. Table 13 reports image-level and pixel-level performance on MVTec-AD, while Table 14 and Table 15 show results for MVTec-3D and VisA, respectively. Our method consistently outperforms existing approaches, demonstrating strong generalization to unseen categories.

Per-Class Quantitative Results in the Single-Class Setting

To support future research and reproducibility, we provide detailed per-class performance of SNARM in the single-class setting on MVTec-AD, MVTec-3D, and VisA. Results are shown in Table 7, Table 8, and Table 9, respectively.

Qualitative Results

Figure 4 visualizes the anomaly maps generated by our method and the baselines on the MVTec-AD dataset under the multi-class setting. As shown, our method accurately localizes anomalous regions across a wide variety of object categories, demonstrating robust localization capability.

Category	P-AP	PRO	P-AUROC	I-AUROC
carpet	88.5	98.9	99.7	99.9
grid	59.3	97.9	99.5	99.8
leather	67.3	98.5	99.6	100.
tile	96.0	97.7	99.6	100.
wood	82.6	96.1	98.1	96.8
bottle	94.8	98.5	99.5	100.
cable	86.3	96.1	99.3	99.5
capsule	60.8	96.5	99.0	97.3
hazelnut	92.1	97.4	99.7	100.
metal_nut	91.2	96.4	98.8	99.9
pill	83.2	98.3	98.7	98.4
screw	54.7	96.4	99.3	98.0
toothbrush	79.4	95.2	99.5	100.
transistor	71.1	87.9	95.0	99.3
zipper	80.8	97.6	99.3	100.
Average	79.2	96.6	99.0	99.3

Table 7: Per-Class Results on the MVTec-AD (Bergmann et al. 2019) Dataset under the Single-class setting.

Category	P-AP	PRO	P-AUROC	I-AUROC
bagel	73.5	98.1	99.5	97.2
cable_gland	66.0	99.3	99.8	97.5
carrot	63.0	99.2	99.8	96.9
cookie	71.1	95.3	98.8	89.2
dowel	64.7	98.2	99.6	98.7
foam	51.2	87.1	95.4	89.6
peach	73.8	99.2	99.8	95.4
potato	50.8	98.4	99.6	80.8
rope	78.9	99.2	99.8	99.5
tire	61.4	97.8	99.6	95.1
Average	65.5	97.2	99.2	94.0

Table 8: Per-Class Results on the MVTec-3D (Bergmann et al. 2021) Dataset under the Single-class setting.

Category	P-AP	PRO	P-AUROC	I-AUROC
candle	54.3	97.4	99.7	99.0
capsules	67.7	97.3	99.7	99.0
cashew	77.6	90.2	99.2	98.6
chewinggum	64.4	89.0	99.3	99.2
fryum	42.5	88.2	95.2	98.4
macaroni1	31.7	97.4	99.8	98.0
macaroni2	20.6	96.3	99.6	90.4
pcb1	85.1	92.2	99.6	98.5
pcb2	40.6	91.8	98.8	97.6
pcb3	52.3	84.2	99.2	99.5
pcb4	48.8	89.5	98.5	98.9
pipe_fryum	79.6	94.4	99.6	99.1
Average	55.4	92.3	99.0	98.0

Table 9: Per-Class Results on the VisA (Zou et al. 2022) Dataset under the Single-class setting.

Method→	DiAD (He et al. 2024b)	MambaAD (He et al. 2024a)	Dinomaly (Guo et al. 2024)	INP-Former (Luo et al. 2025)	SNARM ($T = 10^4$)	SNARM ($T = 10^5$)
Category↓						
carpet	42.2/90.6/98.6/99.4	60.0/96.7/99.2/99.8	68.7/97.6/99.3/99.8	72.5/97.7/ 99.4 /99.9	85.5 / 98.3 / 99.4 / 100 . 87.5 / 98.8 / 99.6 / 100 .	
grid	66.0 /94.0/96.6/98.5	47.4/97.0/99.2/ 100 . 55.3/97.2/99.4/99.9	58.1/ 97.7 /99.4/99.9	56.4/ 97.7 / 99.5 / 100 . 59.3 / 98.1 / 99.5 / 100 .		
leather	56.1/91.3/98.8/99.8	50.3/ 98.7 /99.4/ 100 . 52.2/97.6/99.4/ 100 .	56.3/98.0/99.4/ 100 .	62.5 /98.5/99.6/ 100 . 70.6 / 98.7 / 99.7 / 100 .		
tile	65.7/90.7/92.4/96.8	45.1/80.0/93.8/98.2	80.1/90.5/98.1/ 100 . 76.6/88.3/97.8/ 100 .	96.2 / 97.7 / 99.6 /99.9 95.6 / 97.9 / 99.5 /99.9		
wood	43.3/ 97.5 /93.3/99.7	46.2/91.2/94.4/98.8	72.8/94.0/ 97.6 / 99.8 74.6/93.7/ 97.6 / 99.9	74.9 /93.4/97.2/98.9 78.6 / 95.0 / 98.3 /98.5		
bottle	52.2/86.6/98.4/99.7	79.7/95.2/98.8/ 100 . 88.6/96.6/99.2/ 100 .	88.7/ 97.1 /99.1/ 100 .	92.9 /96.6/ 99.3 / 100 . 93.6 / 97.6 / 99.4 / 100 .		
cable	50.1/80.5/96.8/94.8	42.2/90.3/95.8/98.8	72.0/94.2/98.6/ 100 . 79.3 / 94.4 / 98.8 / 100 .	78.7/94.2/98.5/99.6 82.2 / 95.9 / 99.1 /99.3		
capsule	42.0/87.2/97.1/89.0	43.9/92.6/98.4/94.4	61.4/97.2/98.7/ 97.9 60.3/ 97.7 / 98.8 / 99.0	62.5 /95.3/ 98.8 /94.9 65.9 / 97.4 / 99.3 /96.5		
hazelnut	79.2/91.5/98.3/99.5	63.6/95.7/99.0/ 100 . 82.2/ 97.0 /99.4/ 100 .	81.8/ 97.0 /99.5/ 100 .	91.3 /95.5/ 99.6 /99.9 92.1 / 97.7 / 99.7 /99.7		
metal Nut	30.0/90.6/97.3/99.1	74.5/93.7/96.7/99.9	78.6/94.9/96.9/ 100 . 81.2/95.1/97.5/ 100 .	93.5 / 96.8 / 99.0 / 100 . 91.8 / 96.6 / 99.1 / 100 .		
pill	46.0/89.0/95.7/95.7	64.0/95.7/97.4/97.0	76.4/ 97.3 /97.8/99.1 76.1/ 97.3 /97.7/99.1	82.1 /96.2/ 98.6 / 99.7 80.1 / 98.1 / 98.5 / 99.8		
screw	60.6 /95.0/97.9/90.7	49.8/97.1/ 99.5 /94.7	60.2/ 98.3 / 99.6 / 98.4 61.8 / 97.9 / 99.5 /97.5	48.4/93.1/98.7/93.7 58.6/96.4/99.4/ 97.7		
toothbrush	78.7/95.0/99.0/99.7	48.5/91.7/99.0/98.3	51.5/ 95.3 /98.9/ 100 . 58.3/ 95.9 /99.1/ 100 .	79.2 /92.0/ 99.4 / 100 . 79.2 /94.3/ 99.5 / 100 .		
transistor	15.6/ 90.0 /95.1/ 99.8	69.4/87.0/96.5/ 100 .	59.9/77.0/93.2/99.0 64.0/79.0/94.7/99.7	74.5 /88.1/ 96.6 / 99.8 72.3 / 89.8 / 97.0 /99.6		
zipper	60.7/91.6/96.2/95.1	60.4/94.3/98.4/99.3	79.5 / 97.2 / 99.2 / 100 . 75.8/96.4/99.0/ 100 .	75.2/95.4/98.7/ 100 . 78.0 / 97.4 / 99.2 / 100 .		
Average	52.6/90.7/96.8/97.2	56.3/93.1/97.7/98.6	69.3/94.8/98.4/ 99.6 71.0/94.9/98.5/ 99.6	76.9 / 95.3 / 98.8 /99.1 79.0 / 96.6 / 99.1 /99.4		

Table 10: Per-Class Results on the MVTec-AD (Bergmann et al. 2019) Dataset under the Multi-class setting with P-AP/PRO/P-AUROC/I-AUROC metrics.

Method→	DiAD (He et al. 2024b)	MambaAD (He et al. 2024a)	Dinomaly (Guo et al. 2024)	INP-Former (Luo et al. 2025)	SNARM ($T = 10^4$)	SNARM ($T = 10^5$)
Category↓						
bagel	49.6/93.8/98.5/ 100 .	38.3/92.1/98.5/87.7	59.1/95.9/ 99.3 /90.2 59.5/ 96.9 / 99.3 /92.6	66.4 /96.1/99.2/91.5 69.1 / 97.7 / 99.3 / 95.4		
cable-gland	25.2/94.5/98.4/68.1	39.5/98.4/99.4/94.3	62.5/99.3/ 99.8 /98.1 60.9/ 99.4 / 99.8 / 98.6	62.6 /99.1/99.7/96.1 67.9 / 99.4 / 99.8 / 98.6		
carrot	20.0/94.6/98.6/ 94.4	30.1/98.1/99.4/90.7	44.7/98.4/ 99.7 /91.8 47.0/98.9/ 99.7 /94.3	56.1 / 99.0 / 99.7 /94.2 60.6 / 99.2 / 99.8 / 97.8		
cookie	14.0/83.5/94.3/69.4	39.0/83.6/96.8/61.2	58.8/91.4/98.1/78.2 64.6/92.2/ 98.3 /79.9	72.2 / 95.3 / 98.4 / 87.3 71.7 / 95.3 / 98.3 / 90.9		
dowel	31.4/89.6/97.2/98.0	49.9/97.1/99.6/97.6	66.1 / 98.9 / 99.7 / 99.1 63.0/ 98.9 / 99.7 /99.0	59.3/97.4/99.4/94.0 65.2 / 98.9 / 99.7 / 99.2		
foam	9.6/69.1/89.8/ 100 .	23.4/82.7/95.1/84.0	41.8/ 88.8 / 96.6 /89.1 41.0/ 88.9 /96.3/89.4	44.4 /86.7/95.6/90.2 47.4 /88.7/ 96.4 / 90.3		
peach	27.6/94.2/98.4/58.0	43.2/97.1/99.4/92.8	56.1/98.1/99.6/82.7 63.9/ 99.0 / 99.8 / 96.3	68.6 /98.8/99.7/89.0 75.6 / 99.3 / 99.8 / 95.5		
potato	8.6/93.9/98.0/76.3	17.6/94.8/99.0/66.8	44.5/97.7/99.5/ 80.1 46.4/ 98.2 / 99.7 / 80.1	46.6 /97.6/99.5/70.4 50.6 / 98.4 / 99.6 /79.5		
rope	61.0/96.5/99.3/89.2	52.1/95.5/99.4/97.4	58.4/97.9/99.5/ 99.3 56.6/ 98.7 /99.5/ 99.5	71.2 /98.6/ 99.6 /98.7 73.8 / 98.9 / 99.7 /99.2		
tire	5.9/68.8/91.8/92.7	42.0/97.0/99.5/90.0	58.1 / 99.0 / 99.8 / 97.3 56.3 / 99.0 / 99.8 / 96.5	47.6/96.9/99.4/90.4 54.5/98.0/99.6/92.6		
Average	25.3/87.8/96.4/84.6	37.5/93.6/98.6/86.2	55.0/96.5/ 99.2 /90.6 55.9/ 97.0 / 99.2 / 92.6	59.5 /96.5/99.0/90.2 63.6 / 97.4 / 99.2 / 93.9		

Table 11: Per-Class Results on the MVTec-3D (Bergmann et al. 2021) Dataset under the Multi-class setting with P-AP/PRO/P-AUROC/I-AUROC metrics.

Method→	DiAD (He et al. 2024b)	MambaAD (He et al. 2024a)	Dinomaly (Guo et al. 2024)	INP-Former (Luo et al. 2025)	SNARM ($T = 10^4$)	SNARM ($T = 10^5$)
Category↓						
candle	12.8/89.4/97.3/92.8	23.2/95.5/99.0/96.8	43.0/95.4/ 99.4 / 98.7 43.9/95.6/ 99.4 /98.4	53.5 / 95.9 /99.2/98.0 52.4 / 96.2 / 99.7 / 98.6		
capsules	10.0/77.9/97.3/58.2	61.3/91.8/99.1/91.8	65.0/97.4/ 99.6 / 98.6 67.2 / 98.0 / 99.6 / 99.1	68.3 /96.7/ 99.6 /97.9 66.8/ 98.1 / 99.6 /98.2		
cashew	53.1/61.8/90.9/91.5	46.8/87.8/94.3/94.5	64.5/ 94.0 /97.1/ 98.7 66.2/92.0/97.7/ 98.6	73.1 /85.2/ 98.9 /96.4 68.2 / 94.6 / 98.8 / 98.6		
chewinggum	11.9/59.5/94.7/99.1	57.5/79.7/98.1/97.7	65.0/88.1/99.1/ 99.8 59.6/86.5/98.9/ 99.7	86.0 / 89.3 / 99.3 /99.3 86.4 / 92.6 / 99.5 /99.2		
fryum	58.6 /81.3/ 97.6 /89.8	47.8/91.6/ 96.9 /95.2	51.6 / 93.5 /96.6/ 98.8 51.2/ 94.2 /96.8/ 99.3	47.1/85.6/ 96.9 /98.2 46.6/89.0/96.7/98.5		
macaron1	10.2/68.5/94.1/85.7	17.5/95.2/99.5/91.6	33.5 / 96.4 / 99.6 / 98.0 33.9 /96.0/ 99.6 / 98.5	24.0/93.6/98.9/95.8 20.1/ 97.0 / 99.6 /95.1		
macaron2	0.9/73.1/93.6/62.5	9.2/96.2/99.5/81.6	24.7 / 98.7 / 99.7 / 95.9 26.8 / 98.7 / 99.8 / 96.9	15.9/91.8/95.9/90.5 16.5/97.5/99.4/92.0		
pcb1	49.6/80.2/98.7/88.1	77.1/92.8/ 99.8 /95.4	87.9/ 95.1 /99.5/ 99.1 87.6/ 95.2 /99.6/ 98.8	88.7 /87.1/99.2/96.0 88.2 /94.5/ 99.7 /98.0		
pcb2	7.5/67.0/95.2/91.4	13.3/89.6/ 98.9 /94.2	47.0 / 91.3 /98.0/ 99.3 31.2/ 91.9 / 98.7 / 98.8	44.0 /87.8/97.8/96.1 42.8/89.8/98.6/96.1		
pcb3	8.0/68.9/96.7/86.2	18.3/89.1/ 99.1 /93.7	41.7/ 94.6 /98.4/ 98.9 30.6/ 94.3 /98.8/ 99.2	46.9 /86.0/98.1/97.1 52.9 /90.5/ 99.2 / 98.9		
pcb4	17.6/85.0/97.0/99.6	47.0/87.6/98.6/ 99.9	50.5 / 94.4 / 98.7 /99.8 53.2 / 94.2 / 98.8 / 99.9	42.2/87.4/97.7/98.8 49.3/91.0/ 98.7 /99.1		
pipe_fryum	72.7/89.9/94.9/96.2	53.5/95.1/99.1/98.7	64.3/95.2/99.2/ 99.2 63.3/ 95.8 /99.3/ 99.5	77.9 /94.6/ 99.6 /97.1 75.5 / 96.5 / 99.6 /99.0		
Average	26.1/75.2/96.0/86.8	39.4/91.0/98.5/94.3	53.2/ 94.5 /98.7/ 98.7 51.2/ 94.4 / 98.9 / 98.9	55.6 /90.1/98.4/96.8 55.5 /94.0/ 99.1 /97.6		

Table 12: Per-Class Results on the VisA (Zou et al. 2022) Dataset under the Multi-class setting with P-AP/PRO/P-AUROC/I-AUROC metrics.

Method→ Category↓	CPR (Li et al. 2023a)	HETMM (Chen et al. 2024)	Dinomaly (Guo et al. 2024)	SNARM ($T = 10^4$)
carpet	65.1/92.4/97.1/92.9	67.2/97.2/99.1/99.9	45.2/84.9/95.8/98.0	87.1/98.7/99.7/100.
grid	15.9/74.6/92.1/74.6	48.0/96.6/98.8/96.9	1.6/13.6/47.5/63.8	57.2/98.0/99.5/99.8
leather	66.9/ 99.4/99.6/100.	67.2/98.7/99.7/100.	10.7/34.3/73.7/ 100.	78.7/99.0/99.8/100.
tile	46.6/79.5/89.7/93.4	70.3/90.6/97.3/99.7	46.2/58.0/80.6/92.0	95.7/97.6/99.5/100.
wood	61.7/95.0/95.1/98.8	58.1/ 95.0/96.3/99.7	18.0/23.9/58.8/66.8	78.7/90.9/97.9/96.8
bottle	89.6/97.5/99.1/100.	83.8/96.3/98.8/ 100.	13.8/30.9/73.2/55.0	94.4/98.0/99.5/100.
cable	74.3/88.0/98.3/92.3	67.9/ 94.3/98.6/99.7	6.5/23.5/54.2/52.2	85.0/96.1/99.2/99.6
capsule	46.6/94.3/ 98.8/89.0	50.0/96.4/98.8/100.	4.9/46.5/86.5/46.8	62.7/97.4/99.3/97.6
hazelnut	73.1/95.8/99.1/ 99.3	76.4/96.4/99.4/100.	13.5/39.2/84.3/72.4	90.6/96.5/99.6/98.9
metal_nut	83.1/91.4/96.7/96.0	87.6/94.0/98.3/100.	33.3/48.3/76.0/61.4	96.2/95.9/99.4/100.
pill	50.0/89.0/94.6/73.6	77.0/97.0/98.4/98.7	8.8/47.5/74.8/44.2	81.3/98.0/98.3/100.
screw	35.9/ 96.8/99.3/88.3	53.1/96.5/99.3/93.1	1.4/57.8/87.7/60.4	51.3/96.3/99.3/97.0
toothbrush	60.9/ 95.5/99.1/100.	65.7/94.8/99.4/100.	12.6/40.4/86.8/78.9	72.6/94.8/99.4/100.
transistor	74.0/87.0/94.5/99.5	82.1/96.1/99.0/100.	7.0/17.0/52.6/31.4	66.9/ 87.1/95.5/99.3
zipper	78.1/95.1/98.7/94.8	65.5/ 96.6/98.6/99.7	5.3/27.0/73.7/31.2	78.0/97.1/99.1/100.
Average	61.4/91.4/96.8/92.8	68.0/95.8/98.6/99.2	15.2/39.5/73.8/63.6	78.4/96.1/99.0/99.3

Table 13: Per-Class Results on the MVTec-AD (Bergmann et al. 2019) Dataset under the Cross-class setting with P-AP/PRO/P-AUROC/I-AUROC metrics.

Method→ Category↓	CPR (Li et al. 2023a)	HETMM (Chen et al. 2024)	Dinomaly (Guo et al. 2024)	SNARM ($T = 10^4$)
cable_gland	64.2/97.5/99.0/85.6	52.7/93.2/98.0/ 94.3	1.1/48.2/85.0/46.4	77.8/98.8/99.6/93.1
bagel	7.8/89.9/96.4/69.8	25.8/96.9/98.8/89.0	4.5/50.8/90.0/49.0	75.4/99.7/99.9/97.2
carrot	10.8/95.7/98.7/65.1	27.9/97.7/99.2/87.1	10.2/88.3/97.5/58.8	63.8/99.3/99.8/95.9
foam	22.9/89.9/96.8/60.6	51.5/90.6/97.7/65.3	0.7/26.1/73.1/53.8	75.1/95.7/98.8/89.0
rope	21.4/97.0/ 99.3/90.2	49.6/97.5/99.1/98.3	2.4/54.2/87.0/21.6	72.9/99.3/99.8/99.4
dowel	29.2/83.7/95.3/78.8	28.5/ 86.8/95.6/77.8	3.7/81.2/94.9/52.4	50.3/86.4/94.3/92.6
potato	10.8/92.4/97.6/55.5	31.9/94.5/98.3/79.9	3.0/83.8/95.8/33.3	81.0/99.6/99.9/97.9
cookie	0.5/53.0/84.7/50.2	14.8/96.5/98.9/64.9	8.1/72.5/90.6/50.9	55.7/98.4/99.7/84.2
tire	53.5/90.5/98.4/90.4	60.4/97.8/99.6/98.1	0.4/9.0/68.2/39.4	77.8/98.8/99.8/99.6
peach	14.6/86.1/96.8/67.3	33.6/96.9/99.2/79.6	7.3/80.9/95.5/62.9	59.4/97.0/99.3/96.4
Average	23.6/87.6/96.3/71.3	37.7/94.8/98.4/83.4	4.2/59.5/87.8/46.9	68.9/97.3/99.1/94.5

Table 14: Per-Class Results on the MVTec-3D (Bergmann et al. 2021) Dataset under the Cross-class setting with P-AP/PRO/P-AUROC/I-AUROC metrics.

Method→ Category↓	CPR (Li et al. 2023a)	HETMM (Chen et al. 2024)	Dinomaly (Guo et al. 2024)	SNARM ($T = 10^4$)
candle	25.7/92.4/96.4/ 94.1	29.2/93.0/97.9/87.8	0.7/46.6/81.0/62.6	51.0/94.1/99.6/98.9
capsules	0.3/8.0/47.0/60.7	21.9/82.8/95.5/64.3	0.8/21.8/71.6/62.8	63.6/97.2/99.2/98.0
casewh	63.9/ 88.0/96.3/92.7	65.4/87.9/92.4/91.2	16.4/45.4/82.8/46.6	86.8/92.6/99.8/99.1
chewinggum	64.0/57.8/96.9/97.3	35.4/ 87.3/90.7/92.1	37.6/59.7/95.1/85.1	75.1/90.8/99.5/99.4
fryum	43.8/84.9/95.6/ 91.6	49.7/86.8/95.8/91.0	17.5/56.5/90.5/65.1	50.8/92.6/97.5/99.2
macaroni1	4.4/ 90.2/98.8/83.6	16.1/86.2/95.7/84.1	0.7/63.5/90.8/51.6	27.6/98.6/99.8/98.0
macaroni2	0.6/77.0/ 94.5/66.6	5.5/86.0/94.2/77.9	0.3/56.7/86.9/48.5	17.2/98.3/99.7/92.9
pcb1	38.9/ 95.3/99.0/94.0	83.4/94.1/99.4/96.7	1.8/16.8/82.3/44.2	84.3/93.7/99.5/98.0
pcb2	14.6/ 90.5/99.0/92.5	15.9/89.3/97.9/90.7	5.0/56.8/88.6/56.1	41.4/90.6/98.7/95.9
pcb3	29.3/83.1/98.6/90.7	18.9/ 89.5/98.6/93.0	1.4/47.5/82.8/52.7	51.8/94.0/98.8/98.2
pcb4	12.9/68.0/90.9/97.1	47.6/90.7/98.1/99.7	6.1/63.7/88.3/54.0	44.9/87.1/98.1/99.1
pipe_fryum	71.4/95.1/ 99.3/93.0	71.8/95.3/99.1/98.9	29.6/82.7/95.5/84.3	77.6/96.5/99.7/99.7
Average	30.8/77.5/92.7/87.8	38.4/89.1/96.3/89.0	9.8/51.5/86.3/59.5	56.0/93.8/99.1/98.0

Table 15: Per-Class Results on the VisA (Zou et al. 2022) Dataset under the Cross-class setting with P-AP/PRO/P-AUROC/I-AUROC metrics.

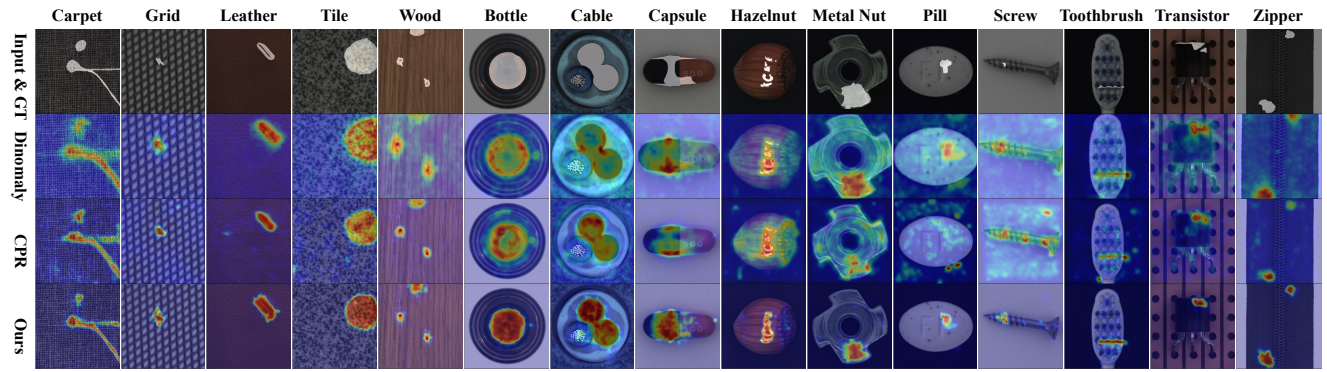


Figure 4: Qualitative results of our SNARM on MVtec-AD under the Multi-class setting. Two SOTA methods (Dinomaly (Guo et al. 2024) and CPR (Li et al. 2023a)) are also involved in the comparison.